Electrical resistivity and elastic wave propagation anisotropy in glancing angle deposited tungsten and gold thin films

Raya El Beainou[1], Asma Chargui[1], Paulo Pedrosa[2], Alexis Mosset[1], Sébastien Euphrasie[1], Pascal Vairac[1], Nicolas Martin[1 *]

[1] *Institut FEMTO-ST, UMR 6174, CNRS, ENSMM, Univ. Bourgogne Franche-Comté, 15B, Avenue des Montboucons, 25030 BESANCON Cedex, France*

[2] *Centro de Física da Universidade do Minho, Campus de Gualtar, Braga, Portugal*

[*] Author to whom correspondence should be addressed. Electronic mail: nicolas.martin@femto-st.fr.

Abstract

We report on experimental investigations of electrical resistivity and surface elastic wave propagation in W and Au thin films sputter-deposited by glancing angle deposition. For both metals, the angle of deposition α is systematically changed from 0 to 85°. Dense and compact films are produced with a normal incident angle α = 0°, whereas inclined and porous columnar architectures are clearly obtained for the highest angles. Group velocities and DC electrical resistivities of W and Au films are significantly changed in *x* and *y* directions as α increases from 0 to 85°. Isotropic behaviors are always observed for Au films, whereas anisotropic velocity and resistivity are clearly measured in W films prepared with incident angles higher than 60°. The anisotropic coefficient reaches 1.8 for velocity and 2.0 for resistivity in W films, while it remains in-between 1.0 – 1.2 in Au films whatever the incident angle. This directional dependence of electrical resistivity and elastic wave propagation is connected to the anisotropic structural characteristics of W inclined columns (fanning of their cross-section), while Au columns exhibit a more symmetric growth as a function of the incident angle.

Keywords

Glancing Angle Deposition; Tungsten; Gold; Columnar films; Surface acoustic wave; Resistivity; Anisotropy.

1 Introduction

How elastic wave and electron propagations in bulk ordered materials are affected by the crystal symmetries has been and is still a topic of great interest over the past few decades. Such interest is mainly motivated by understanding and controlling the transport mechanisms as a challenging task for a wide variety of applications in areas such as gas sensors, surface acoustic wave (SAW) devices, semiconductors and so on [1, 2]. Assuming that most of single crystalline solids exhibit direction-dependent properties due to an intrinsic anisotropy at the atomic scale (directional differences coming from inter-atomic stiffness bonds in the crystal structure), anisotropic behaviors may vanish when the material adopts a polycrystalline structure. Reducing the effective dimensionality of a material from 3D to 2D, is one strategy that is expected to enhance the anisotropy of a material's physical properties including those related to elastic wave–matter and electron-matter interactions. Therefore, the anisotropic properties may become significant in thin film materials and surfaces since these nearly 2D systems can develop a wide panel of textures and architectures, particularly at the micro- and nano-scales [3, 4]. In this case, such surfaces actually consist of randomly organized architectures per unit area, with direction dependent geometrical features that produce directionally dependent physical properties.

The fabrication method obviously influences the resulting patterning. In this way, thin films prepared by conventional sputtering processes typically exhibit isotropic properties. Many studies reported graded characteristic through the film thickness [5, 6], but very little have been focused on the asymmetric physical properties of the film surface [7, 8]. In thin film deposition, some specific techniques allow producing anisotropic structures. The GLancing Angle Deposition (GLAD) approach is among the most attractive ways to produce original surface morphologies, especially to tune the surface anisotropy [9-11].

This approach for designing anisotropic architectures in thin films becomes particularly interesting since the property in question arises solely from the ground state microstructure, rather than any lattice asymmetry. In the GLAD technique, the microstructural anisotropy can be changed as a function of the incident angle of the particle flux or azimuthal position of the substrate holder [12, 13], the sputtering pressure [14, 15], and more recently by means of the GLAD co-deposition of more or less miscible metals to create Janus-like columnar structures [16, 17]. To the best of our knowledge, very few studies [18] have been devoted to the influence of the material nature on the anisotropic growth and their resulting physical properties.

In an earlier publication [19], we reported on the surface elastic wave propagation (surface acoustic wave) in W thin films sputter-deposited by conventional sputtering with a classical microstructure (columns normal to the film-substrate interface) and with a single example of oriented columnar microstructures. Experimental results showed an isotropic behavior of elastic waves in the classical microstructure, whereas an anisotropic elastic wave velocity was measured and simulated (with the Finite Element Method – FEM) in W films exhibiting tilted columns. Some strong connections with the films' microstructure were clearly demonstrated. We present herein a study focused on understanding anisotropic properties in terms of electrical resistivity and elastic wave propagation in nanostructured thin films exhibiting a tilted columnar architecture fabricated by GLAD sputtering. To this aim, two metals have been investigated: W and Au. The choice of these metals has been dictated by their propensity to create a diverse array of columnar morphologies through modifications of their growth conditions due to their nature. It is shown that W GLAD films growth gives rise to tilted columns with a significant fanning of the column cross-section, whereas Au GLAD films deposition produces rather circular (and so more

isotropic) column sections. Correlations between the film's microstructure and their anisotropic behaviors regarding their electronic transport properties and elastic wave propagation are presented. The evolution of the W and Au film characteristics as a function of the column angle is finally discussed and associated with the asymmetric features, as well with the porous morphology.

2 Materials and Methods

W and Au films were deposited by DC magnetron sputtering on glass substrates and (100) Si wafers. The metallic W and Au targets (51 mm diameter and 99.9 at. % purity) were sputtered with a constant current intensity I_W = 200 mA and I_{Au} = 20 mA, respectively. The 40 L homemade sputtering chamber was pumped down using a turbo-molecular pump backed by a primary pump, leading to a residual vacuum close to 10^{-6} Pa. An argon sputtering pressure of $3.0\text{-}3.5\times10^{-1}$ Pa (argon flow rate of 2.3 cm^3min^{-1} and a constant pumping speed of 13 Ls^{-1}) was used during all depositions. No external heating was applied during the growth stage and depositions were performed at room temperature. The deposition time was adjusted so as to get an average film thickness of 500 nm. The GLAD technique was implemented in order to produce normal and tilted columnar architectures. It consists of depositing thin films under an oblique incident flux of the sputtered particles using a fixed or mobile substrate. In this study, the incident angle α was 0, 60, 70, 80 and 85° for W and Au. The substrate holder was stationary (ϕ = 0 rev h^{-1}). The target-to-substrate distance (from center-to-center) was 65 mm. Using such sputtering conditions and assuming Sit *et al.* investigations [20], we assume that the half-width of the sputter flux distribution is about 10° for both metals.

Scanning electron microscopy (SEM) was used to view the surface and the fractured cross-section of the films with a JEOL JSM 7800 field emission microscope. The films were also characterized by X-ray diffraction (XRD) using a Bruker D8 focus diffractometer with a cobalt X-ray tube (Co $\lambda_{K\alpha 1}$ =1.78897 Å) in a θ/2θ configuration with a step of 0.02° per 0.2 s and a 2θ angle ranging from 20 to 80°. The electrical resistivity at room temperature was measured by the four-probe van der Pauw method. The measurements were carried out on glass substrates in air using a custom-made chamber, which was covered in order to achieve a dark environment. The error associated to all resistivity measurements was always below 1% and the attachment of the contacts was checked prior to every run (I/V correlation close to 1) to ensure that an ohmic contact was obtained (use of gold-coated tips). The Bierwagen procedure was used to obtain the anisotropic electrical resistivity of the films, as described in [21]. Measurements of the elastic waves propagation were carried out with a femtosecond pump-probe setup. The system has been previously described in detail [19]. Briefly, it consists in measuring the surface reflectivity change induced by elastic and thermal effects due to the optical absorption of a laser (the pump). A second laser (the probe) measures this reflectivity variation. The temporal reflectance response of the film was obtained with the asynchronous optical sampling (ASOPS) technique. Such conditions allow a whole time spanning of 21 ns with a resolution of about 1 ps. The central wavelength of both beams is 515 nm (frequency doubled Yb:YAG lasers) and they are focused on the sample surface with a spot size of 1 μm. The dispersion curves can be obtained by plotting the FFT-2D (2 dimensions discrete Fourier transform) of the relative reflectivity as a function of the time and position. The slope of the dispersion curve directly leads to the elastic wave group velocities. Velocities are given at the most intense normalized reflectivity of the pseudo-Rayleigh mode ($k/2\pi = 3\times10^5$ m^{-1}). More details can be found in [19].

3 Results and Discussion

3.1 Morphology and structure

W and Au films sputter-deposited by the conventional sputtering process (incident angle $\alpha = 0°$) exhibit typical surface and cross-section morphologies of metallic films as shown from SEM observations (Fig. 1).

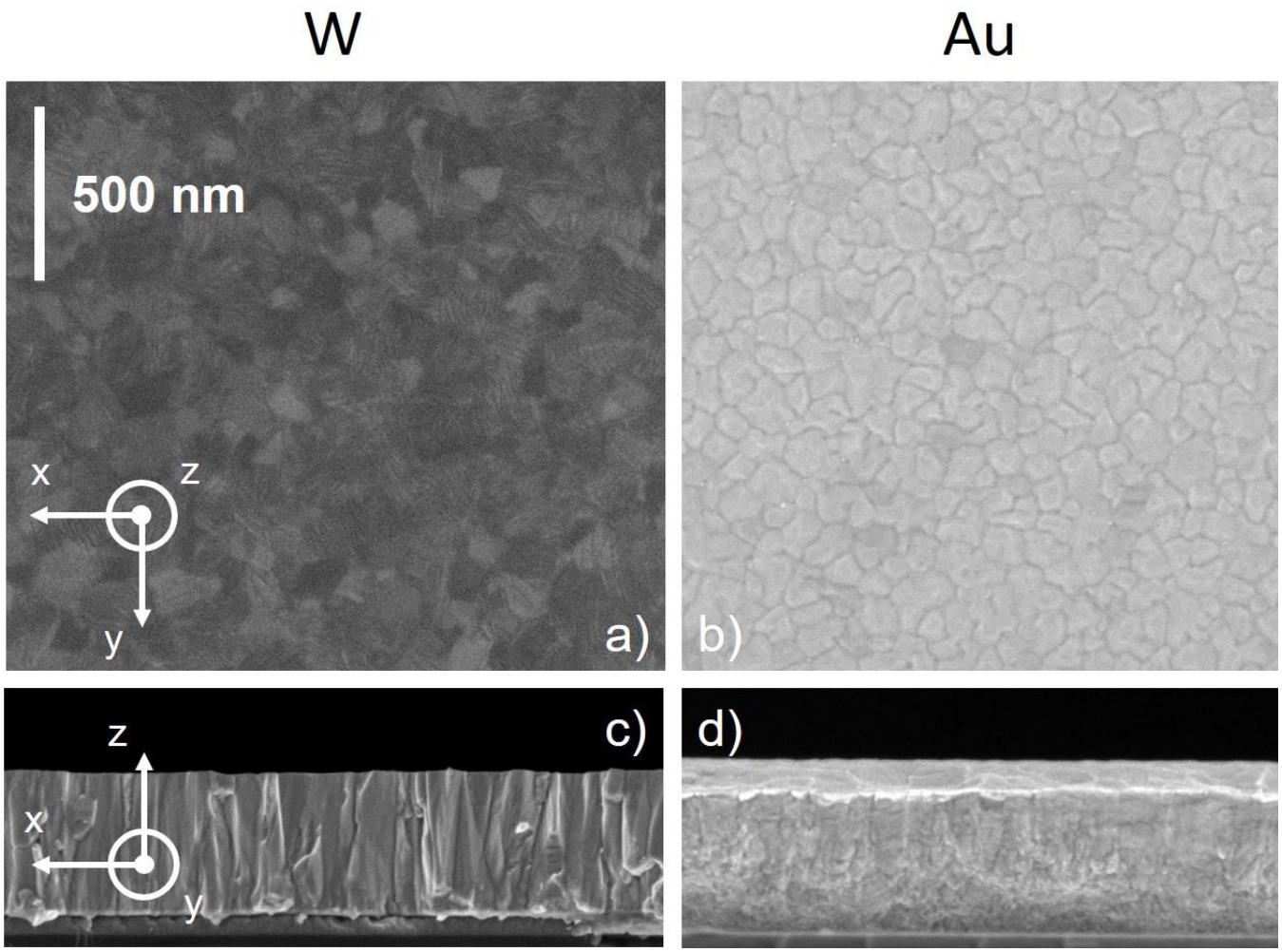

Fig. 1. SEM observations of surfaces (a and b) and cross-sections (c and d) of 500 nm thick W (a and c) and Au (b and d) thin films sputter-deposited by DC magnetron sputtering with a normal incidence of the particle flux (α = 0°). The scale bar is the same for all pictures.

A smooth and columnar microstructure is clearly viewed for W films. This kind of microstructure correlates with the first zone of the structure-zone models (SZM) commonly reported in the literature for sputter-deposited coatings [22-24]. Based on the substrate temperature-to-melting point ratio of the deposited material (T_S/T_M), also called the homologous temperature, such a ratio is lower than 0.1 for W films prepared with our operating conditions (argon sputtering pressure = $3.0\text{-}3.5\times10^{-1}$ Pa and no external heating of the substrate). The microstructure is unsurprisingly columnar and consists of inverted cone-like units capped by domes. Sputtered W are heavy atoms with a limited adatom motion on the growing film. Thus, a quit dense thin film is obtained. For the Au films prepared with the same sputtering conditions as W, T_S/T_M = 0.25. These operating conditions tend to produce a film morphology corresponding to the transition zone, namely zone T, of SZM [25]. The columnar microstructure is less evident for Au films (also due to a less brittle fracture than W films). The surface diffusion is favored, and the top view exhibits a more granular aspect in Au than W films (Fig. 1b).

When the GLAD process is applied to W and Au films, both metals clearly show an inclined columnar and porous structure (Fig. 2). The SZM recently proposed by Mukherjee and Gall [26] for extreme shadowing conditions seems to be more suitable for GLAD films. Assuming a homologous temperature T_S/T_M of 0.1 and 0.25 for W and Au depositions, respectively, one can expect more tiny and fibrous columns for W films. It is in a quite good agreement with the SEM pictures shown in Fig. 2, where Au columns are more connected to each other due to a larger surface diffusion of Au sputtered particles

connected to a higher homologous temperature than W. The high column angle obtained for Au compared to W is also related to the self-diffusion length of atoms impinging on the growing film. The self-diffusion length Λ of atoms is related to the surface diffusion activation energy E_d following [27]:

$$\Lambda = \frac{1}{2}\sqrt{\frac{a_h^2 a_d \omega}{r}}\sqrt{exp\left(\frac{-E_d}{k_B T}\right)} \quad (1)$$

where a_h is the average distance between atoms, i.e. close to the lattice spacing (m), a_d the distance of adatom moving from one adsorption site to another one (m), ω the lattice vibration frequency (s^{-1}), r the deposition rate (m s^{-1}), k_B the Boltzmann constant(1.38×10^{-23} J K^{-1}) and T the surface temperature (K). Since the surface self-diffusion energy for Au and W is 0.347 eV and 3.10 eV, respectively [28, 29] and assuming that all other deposition parameters remain constant, the self-diffusion length of Au is higher than that of W, which leads to a higher column angle in Au films. Based-on a thermalized activated process of the surface self-diffusion, where the pre-exponential factor of Au is systematically lower than that of W, the surface self-diffusion constant of Au is several orders of magnitude higher than that of W. For W films, the shadowing effect inherent to the GLAD technique prevails, whereas for Au films, the surface diffusion of sputtered atoms becomes significant since T_S/T_M = 0.25. This ratio is below the nanostructuring temperature threshold (around 0.33 for metal [30]), above which adatom surface diffusion becomes large enough that a nanorod morphology is no longer formed during the growth [31].

Other parameters may also influence the resulting morphology and microstructure of W and Au GLAD films. The divergence angle of sputtered materials can be substantial for our operating conditions (half-width of the sputter flux distribution is estimated to be about 10° for both metals), and the sputtering pressure used for this study ($3.0\text{-}3.5\times10^{-1}$ Pa) corresponds to a mean free path of particles close to 20 mm.

This length is lower than the target-to-substrate distance (65 mm). Consequently, collisions between argon species and sputtered particles occur and lead to a significant thermalization effect of the sputtered particle energy (the thermalization degree calculated from [32] is about 0.5 Pa^{-1} m^{-1} for both metals). Such effect reduces the average energy per deposited particle, which becomes important when the incident angle α increases and tends to 85°.

It is also worth mentioning that the dragging mechanism previously reported by Alvarez *et al.* [33] also influences the column growth. This mechanism is responsible for mobilizing surface atoms in the direction of the particle flux. It compensates the natural tilt of the columns and straighten them up. Taking into account that the dragging mechanism is caused by the arrival of energetic particles on the top of the growing columns and assuming that W atoms are heavier than Au atoms, tilted columns are produced for both metals with column angles $\beta_{Au} > \beta_{W}$.

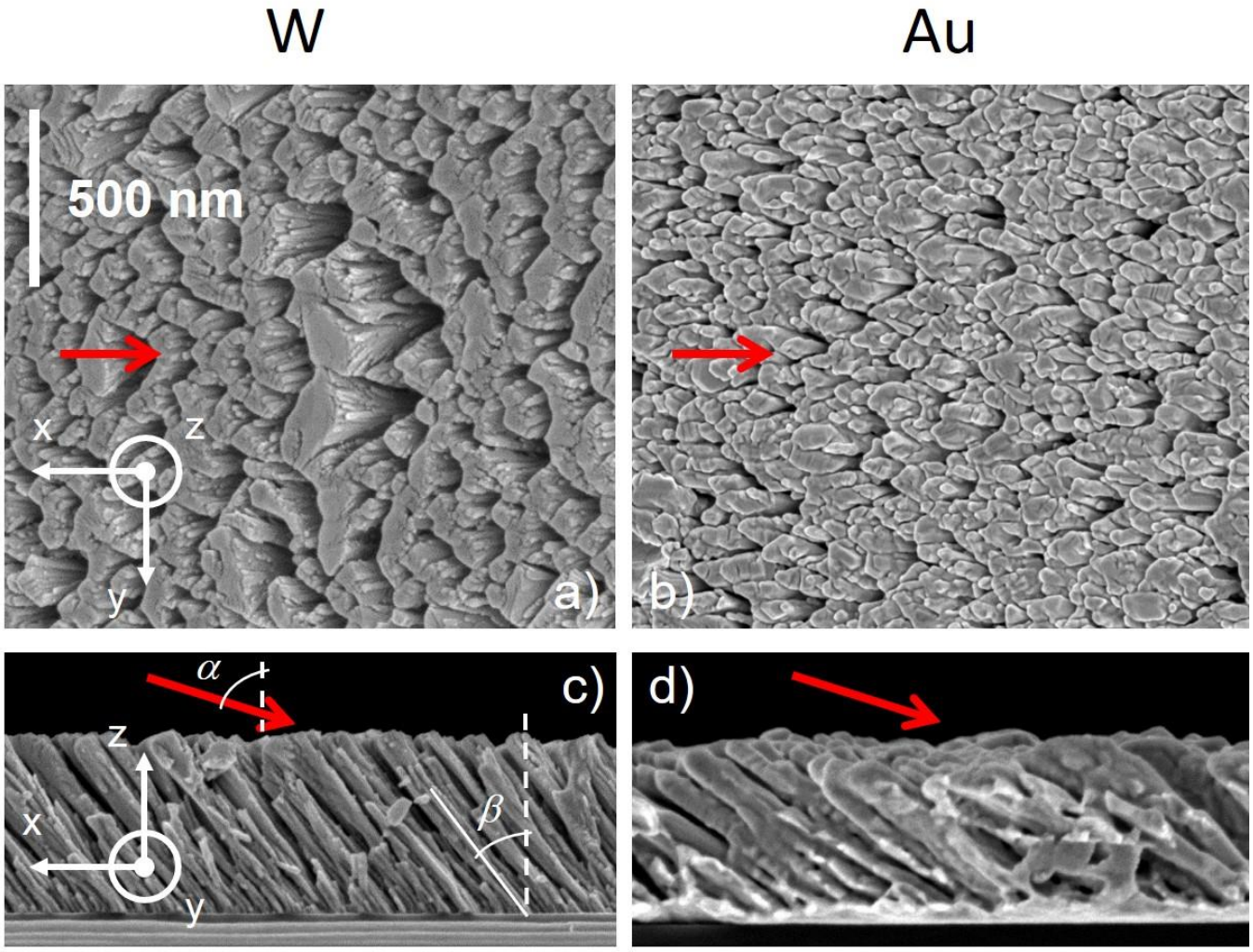

Fig. 2. SEM observations of surfaces (a and b) and cross-sections (c and d) of 500 nm thick W (a and c) and Au (b and d) thin films sputter-deposited by GLAD with an incident angle α = 80°. Red arrows indicate the incoming flux of W or Au atoms, which leads to an inclined columnar architecture. Column angle β = 41° and 57° for W and Au films, respectively. The scale bar is the same for all pictures.

However, the surface morphology is clearly different, as shown in figures 2a and 2b. Top view of Au films exhibits a nodular aspect of the surface with columns more or less connected to each other, randomly distributed and oriented in the direction of the particle flux (Fig. 2b). It is also interesting to note that

column apices distinctly show multiple sub-columns, which are quite bundled and separated by voids. This surface morphology correlates with the limited shadowing mechanism and the surface diffusion of sputtered particles, which becomes significant for Au.

A transverse growth is instead observed for W films (Fig. 2a). As previously argued, a low self-diffusion length of W atoms and a high melting point favors the shadowing effect. Columns are able to grow along the *y*-direction (perpendicular to the particle flux) giving rise to a fanning of the column cross-section. The latter becomes increasingly elliptical (more precisely crescent-shaped) as deposition continues and an anisotropic structure is produced. Such structural anisotropy has also been reported for other GLAD films [21, 34] and occurs for incident angles higher than 60°. Columns are connected to each other by chains, perpendicular to the plane of incidence [35].

The morphological differences between W and Au surfaces can be formally discussed taking into account a power law scaling approach. It was previously shown that the width W of isolated columns increases as a function of deposition time, and so, as a function of column length d, in a power law form, $W \propto d^{p}$, where p is the scaling exponent (describing how quickly the columns broadens), with values in-between 0.3-0.5 for GLAD films, depending on the incident angle α [36]. In addition, the average column sizes in the *x* (parallel to the particle flux) and *y* (perpendicular to the particle flux) directions evolve differently between W and Au due to the competition between shadowing effect and surface diffusion [37]. Shadowing prevails for W films and tends to make columns grow wider. Diffusion makes columns grow towards the columnar axis for Au films. As a result, the shadowing dominated effect produces a lateral growth and allows neighboring columns to merge and chain together. This leads to bundling of the W columnar microstructure in the *y* direction and thus, a structural anisotropy occurs. For W films sputter-

deposited with our operating conditions, the scaling exponents p_x and p_y in the directions parallel and perpendicular to the particle flux, respectively, were determined from SEM observations of the columnar cross-sections *vs.* thickness (not shown here). A significant difference was clearly observed with $p_x = 0.13$ and $p_y = 0.32$. These results correlate with Belyaev *et al.* Monte Carlo simulations [38]. The authors showed that the correlation lengths ξ_x and ξ_y, which refer to the column widths in x and y directions, respectively, evolve differently for glancing incidence angles ($\alpha > 60°$) especially when the shadowing effect prevails during the growth phase. It supports again that elongated column cross-sections are expected perpendicularly to the deposition plane. Assuming the Kardar-Parisi-Zhang (KPZ) equation [39], the scaling exponents parallel p_x and perpendicular p_y to the deposition plane are 1/3 and 2/3, respectively, for a diffusion-limited process (W films). Increasing the surface diffusion effects, p_x reduces more than p_y (3/8 against 1/4, respectively [39]), which rather corresponds to the deposition of GLAD Au films and so to an isotropic growth.

Long range crystalline order and preferential orientation of GLAD W and Au films are noticeably influenced by the incident angle α, as shown from X-ray diffraction patterns in Fig. 3. For both metallic films prepared by the conventional sputtering process ($\alpha = 0°$), a strong preferential orientation along (210) and (111) planes is shown for W and Au films with a crystallite size of 28 nm and 43 nm, respectively (calculated from the Scherrer equation). In vapor-deposited thin films, the preferred orientation can originate from several sources. According to van der Drift [40], three principal parameters may produce texture in thin films: (i) an initial preferred orientation during the first growing stage, (ii) a recrystallization orientation (due to post-deposition annealing), and (iii) an evolutionary or competitive

selection of initially random nucleation. In our study, films were prepared on glass and (100) Si substrates without any pre-seeding or post-annealing treatment. As a result, the loss of crystallinity and the change of preferential orientation simultaneously recorded for W and Au films as the incident angle α increases, have to be connected to the evolutionary selection. Increasing the incident angle of the particle flux, the deposition rate decreases, as well as the energy per deposited particle.

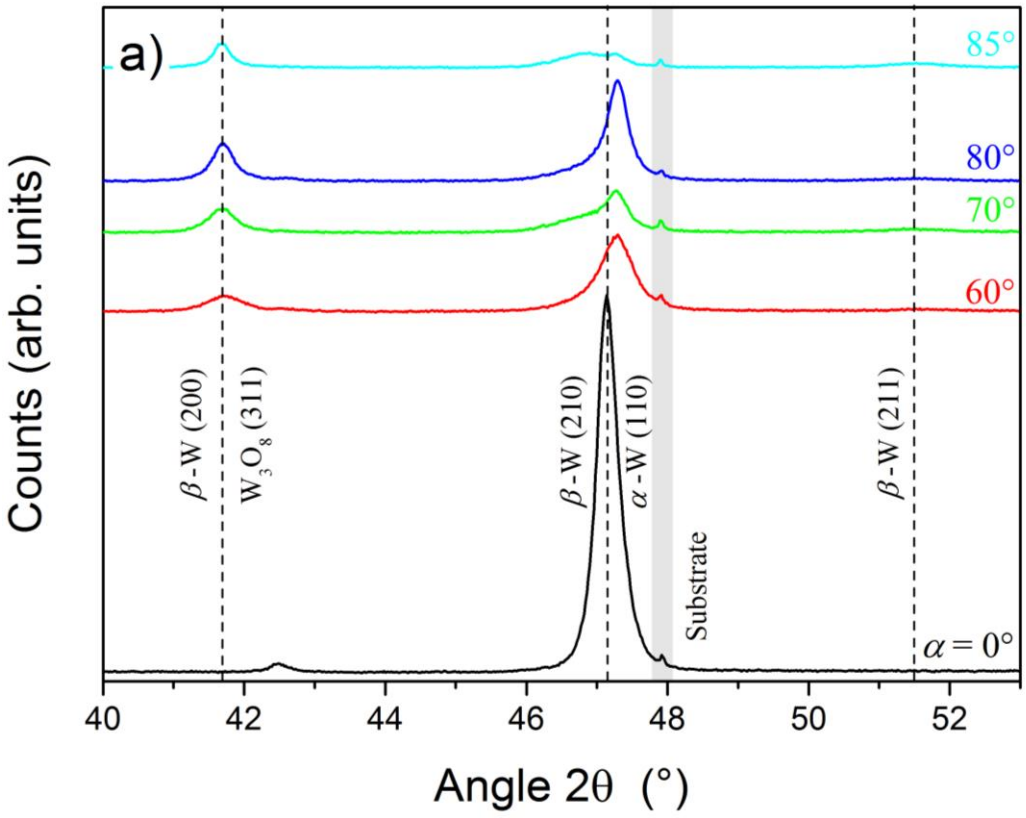

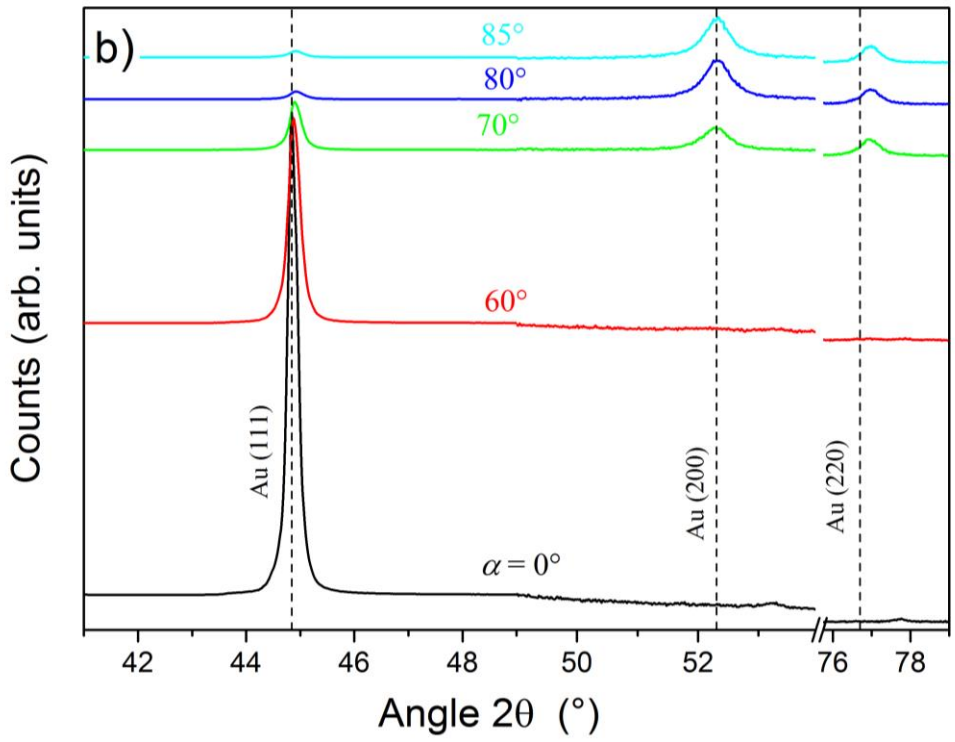

Fig. 3. X-ray diffraction patterns of a) W films and b) Au films prepared on (100) Si and for various incident angles α.

In addition, it favors the directional diffusion of adatoms impinging on the growing film due to the conservation of their momentum (higher momentum parallel to the substrate surface). Moreover, as the incident angle tends to grazing incidence (α > 70°), shadowing effect predominates. The preferred orientation in W and Au films vanishes, which also corresponds to a smaller crystallite size (a few nanometers for both metals). This evolution of the W and Au films preferential orientation is in agreement with previous investigations focused on crystal structure of Ti films prepared at various incident angles [33]. These results also agree with a reduction of the average grain size with the decrease of the energy per incident atom [41]. Increasing the incident angle, the amount of thermalized sputtered particles

reaching the growing film prevails over the ballistic ones. Energy per deposited atom reduces and leads to a lower crystal quality. This loss of long-range order also correlates with the morphology and porosity changes connected to the transition from compact films ($\alpha < 60°$) to a highly porous microstructure when α angle tends to 85° [33]. It means that the grain boundaries density as well as the growth of defects inside the columns are favored for high incident angles. It is worth noticing that diffracted signals corresponding to the β-W phase are also recorded for W films prepared with an incident angle α higher than 60°. Due to the very close position at 2θ = 46.76° of the (210) peak and at 2θ = 47.12° of the (110) peak related to β (card #65-6453) and α (card #04-0806) phases, respectively, the precise crystallographic structure of these films still remains an open question. One can only suggest the growth of a phase mixture for such sputtering conditions. These results agree with former studies [42-44] reporting the development of bcc α and A15 β phases in sputter-deposited W thin films. Oxygen incorporation in W films favors the stabilization of the β-W phase. A voided structure is enhanced as the incident angle α rises. So, we can expect the formation of this β phase in W GLAD films. In addition, films become more sensitive to oxygen and tungsten oxide compounds may also be produced such as the W_3O_8 phase (card #65-1175) with the (311) peak at 2θ = 41.81°, or the β-W phase with the (200) peak at 2θ = 41.58°.

3.2 Electrical properties

Average DC electrical resistivity measured at room temperature ρ_{300K} of W and Au GLAD films deposited on glass is also influenced by the incident angle (Fig. 4). Films prepared with normal incidence ($\alpha = 0°$) exhibit resistivity values of 1.3×10^{-7} Ω m and 3.0×10^{-8} Ω m for W and Au, respectively. As commonly

observed in sputter-deposited thin films, it is slightly higher than that of bulk materials since ρ_{300K} (W) = 5.4×10^{-8} Ω m and ρ_{300K} (Au) = 2.3×10^{-8} Ω m for bulk [45]. This difference is usually attributed to the grain boundary scattering of conduction electrons. Due to the polycrystalline structure of thin films, the electron mean free path is restricted by the crystallite size. If the latter is lower than the electron mean free path, many instances of electron scattering occur at the grain boundaries, which decreases the conductivity. Since the electron mean free paths in W and Au (16 nm and 38 nm, respectively [46]) are both in the same order of magnitude of the crystallite size calculated from XRD patterns (cf. § 3.1), it is normally expected a higher resistivity in polycrystalline thin films than in bulk materials, especially when a columnar microstructure is produced.

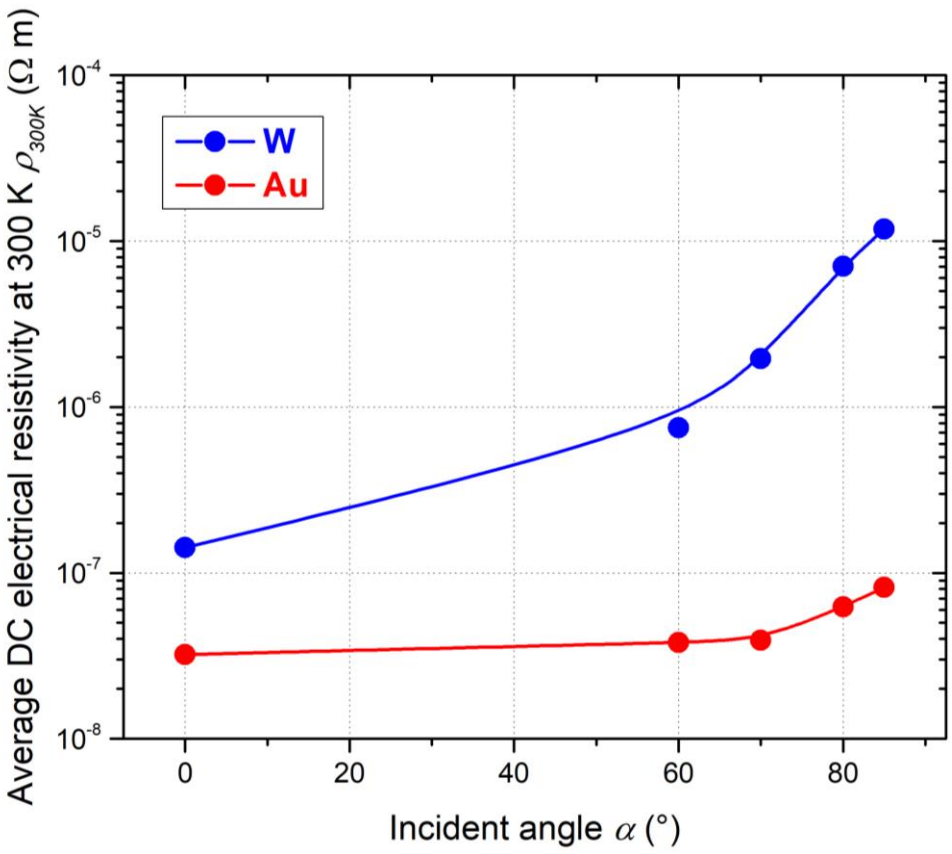

Fig. 4. Average DC electrical resistivity ρ_{300K} measured at 300 K as a function of the incident angle α for 500 nm thick W and Au thin films sputter-deposited by GLAD on glass (error bars are not specified and meaningless).

Increasing the incident angle up to $\alpha = 60°$ leads to a negligible change of Au films resistivity, whereas that of W films significantly rises to 7.5×10^{-7} Ω m (Fig. 4). Until this range of incident angles, the morphological microstructure (not shown here) of Au and W films does not meaningfully change compared to those observed at normal incidence, i.e. a quite dense and granular aspect for Au films with no clear feature from the cross-section view and a dense and slightly inclined columnar structure (a few degrees) for W films. As a result, the substantial increase of resistivity especially measured for W films

and the constant electrical properties of Au films produced at $\alpha = 60°$ can be connected to the reduction of the crystallite size, as illustrated from XRD patterns in figure 3. From the most intense diffracted signal ((210) for W and (111) for Au), the crystallite size (again determined from the Scherrer equation) exhibits a small decrease from 43 nm to 38 nm for Au films as the incident angle α changes from 0° to 60°, whereas it drops from 28 to 19 nm for W films. As a result, scattering of electron conduction at the grain boundaries is more prominent in W films, which promotes the increase of electrical resistivity values when compared to Au films.

For both metals, the films resistivity mainly increases for incident angles higher than 60°. For the highest incident angle $\alpha = 85°$, the films resistivity reaches 1.2×10^{-5} Ω m and 8.2×10^{-8} Ω m for W and Au films, respectively. These results are in agreement with former investigations devoted to GLAD metallic films [47-49]. The α dependence is very similar across each metal with a slow resistivity increase at low incident angles, followed by a step change at higher α values. This general trend is mainly assigned to the microstructural changes caused by ballistic shadowing at oblique incidence. Whatever the material, tilted columnar GLAD films can be viewed as an oriented mixture of conducting (metal) and insulating (void region) phases. By depositing at high incident angles ($\alpha > 60°$), the void fraction of the films becomes substantial, which reduces the number of conducting paths through the films and thus, the electrical resistivity increases. A theoretical model recently proposed by Besnard *et al.* [47] supports this rise of resistivity *vs.* incident angle. The authors clearly showed that the sudden increase of resistivity is obtained for a given column angle β and thus incident angle α. Such increase is mainly assigned to the evolution of the film's density as a function of the incident angle. A more porous structure is favored as the incident

angle rises, especially for angles higher than 70°. So, the high resistivity is attributed to the enhancement of electron scattering by surfaces and grain boundaries induced by a more voided microstructure promoted as the α angle tends to 85°.

It is also worth noting that two orders of magnitude are measured between resistivity at α = 0 and 85° for W films, whereas it remains in-between 10^{-8}-10^{-7} Ω m for Au films. This difference between W and Au is related to the more porous structure certainly produced in W films. Since the shadowing effect prevails in W films growth, whereas surface diffusion phenomenon becomes significant in Au films, one can expect a more voided columnar structure in W films. In addition, stating that W is more reactive towards oxygen than Au and combining a more porous architecture, W tilted columns are certainly oxidized, which increases even more the films resistivity [50, 51].

Electrical resistivities of the films following *x* and *y* directions (determined from the Bierwagen method [21]) are quite similar for W and Au films prepared by conventional sputtering, i.e. in the order of 10^{-7} and 10^{-8} Ω m for Au and W films, respectively (Table 1). Conversely, W GLAD films prepared with α = 80° exhibit a higher resistivity along the *x* direction, whereas Au GLAD films do not exhibit so significant electrical resistivity anisotropy. This difference between ρ_x and ρ_y is again related to the GLAD film microstructure. A very high porous architecture is favored for grazing incident angles of the particle flux and so, the number of electrical pathways available for the free carriers is reduced. This leads to a decrease of the electron mean free path.

Table 1. DC electrical conductivity at 300 K and group velocities of pseudo-Rayleigh waves at $k/2\pi = 3\times10^5$ m^{-1} along x and y directions in Au and W thin films sputter-deposited with a normal incident angle ($\alpha = 0°$) and by the GLAD technique ($\alpha = 80°$).

Material	Incident angle α (± 2°)	Column angle β (± 3°)	DC electrical resistivity ρ at 300 K (S m^{-1})		Group velocity v at $k/2\pi = 3\times10^5$ m^{-1} (± 50 m s^{-1})	
			x axis ρ_x	*y* axis ρ_y	*x* axis v_x	*y* axis v_y
Gold (Au)	0	0	3.03×10^{-8}	2.91×10^{-8}	1710	1730
	80	57	9.14×10^{-8}	7.20×10^{-8}	1230	1180
Tungsten (W)	0	0	1.33×10^{-7}	1.30×10^{-7}	2220	2260
	80	41	1.57×10^{-5}	7.83×10^{-6}	920	1640

In addition, GLAD deposition of columnar films with incident angles higher than 60° gives rise to a significant structural and uniaxial anisotropy in the substrate plane induced by the shadowing effect. As a result, an anisotropic distribution of the grain boundary potential barrier heights is produced for W films (less evident for Au films). This effect mainly occurs in the direction of the incident vapor flux (*x* direction). Islands grow with connections to each other by chains perpendicular to the plane of incidence or to the direction of shadowing effect (*y* direction). Films grow according to a columnar structure with columns exhibiting an elliptical section, which is particularly marked for W films prepared with α = 80° (Fig. 2a). Anisotropic growth due to the GLAD process with predominance of the shadowing effect, intrinsically leads to the highest grain boundary potential barriers in the *x*-direction in comparison with the *y*-ones. Therefore, difference of electrical resistivity in the orthogonal axes is more noticeable in W

than Au GLAD films [15, 17]. It is interesting to notice that the anisotropic behavior of resistivity of W films agree with Song *et al.* investigations [52]. They recently proposed a model describing the anisotropic electronic transport in tilted silver nanorod arrays produced by oblique angle deposition. Anisotropy results from the difference in node connectivity parallel with and perpendicular to the nanorod tilting direction, and thus to the incoming particle flux.

3.3 Elastic propagation

The relative variation of W and Au films reflectivity *vs.* time and the distance between the pump and probe beams following the *x* (parallel to the incoming particle flux) and *y* (perpendicular to the incoming particle flux) directions was measured by the femtosecond pump-probe setup [19] for both metals sputter-deposited with incident angles α between 0 and 85°. The dispersion curves were obtained by computing the 2D-FFT (2 Dimensions Fast Fourier Transform) of the aforementioned variations and plotted for α = 0 and 80° (Fig. 5 and 6).

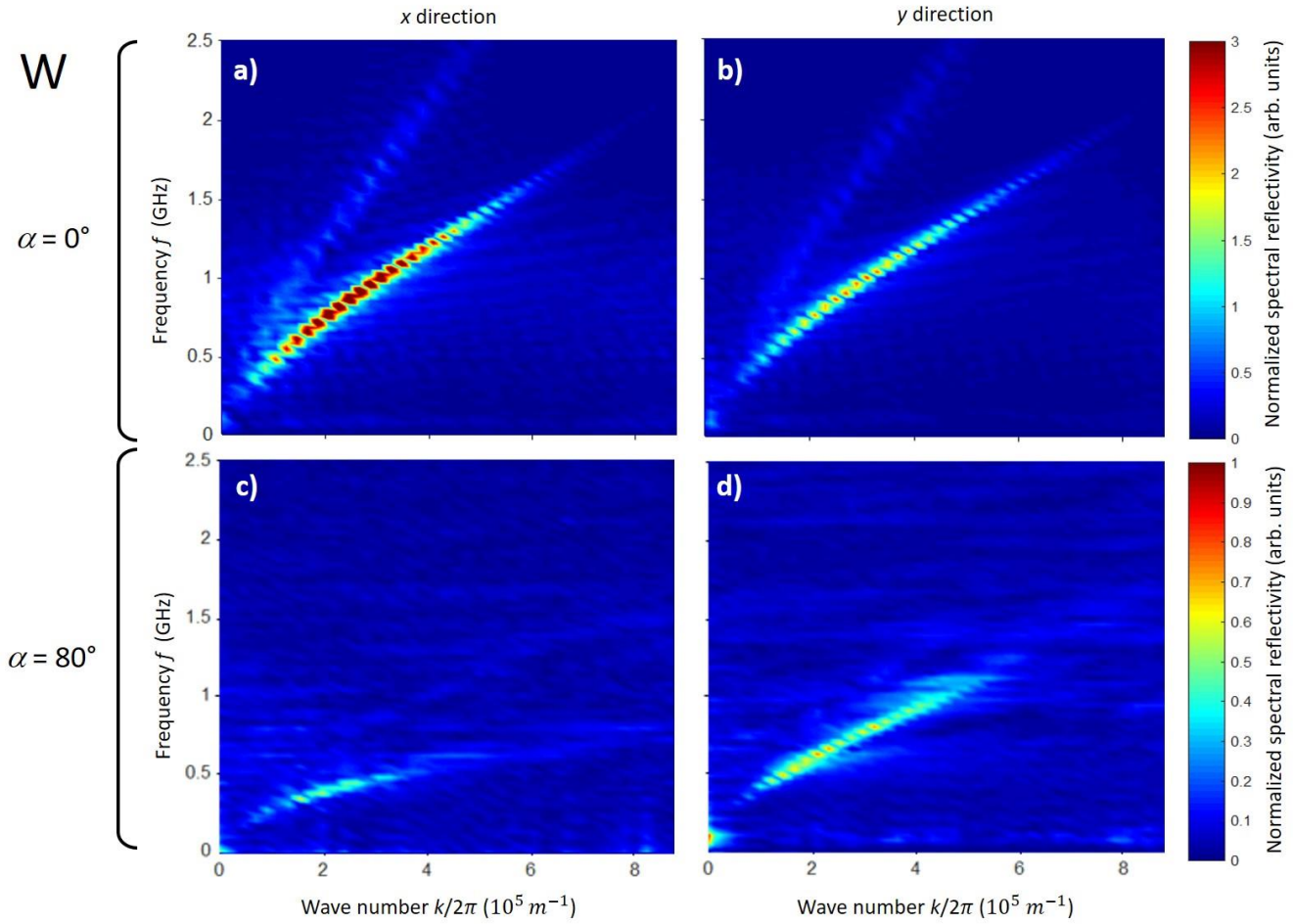

Fig. 5. Dispersion curves in W films for x (a and c) and y (b and d) directions obtained from the variation of the relative reflectivity vs. spatial and time frequencies for α = 0° (a and b) and α = 80° (c and d). Frequencies and wave numbers corresponding to the highest power spectral density (dark red level on normalized spectral reflectivity scale) have been used to determine the elastic wave group velocities.

For conventional W and Au films ($\alpha = 0°$) and for both *x* and *y* directions, pseudo-Rayleigh are the most intense elastic waves. Note that for W films prepared with $\alpha = 0°$, surface-skimming longitudinal and Sezawa modes cannot be clearly distinguished from our *x* and *y* dispersion curves (both are superimposed and very close to each other), whereas the Sezawa mode is rather measured for Au films (the signal-to-

noise ratio however remains weak). The pseudo-Rayleigh waves exhibit a dispersive behavior since the frequency *vs.* wave number plots systematically exhibit a nonlinear characteristic. One can claim an isotropic in-plane behavior for these films, which could be expected since the conventional sputtering process ($\alpha = 0°$) leads to a quite dense, columnar and homogeneous microstructure (as previously shown in Fig. 1).

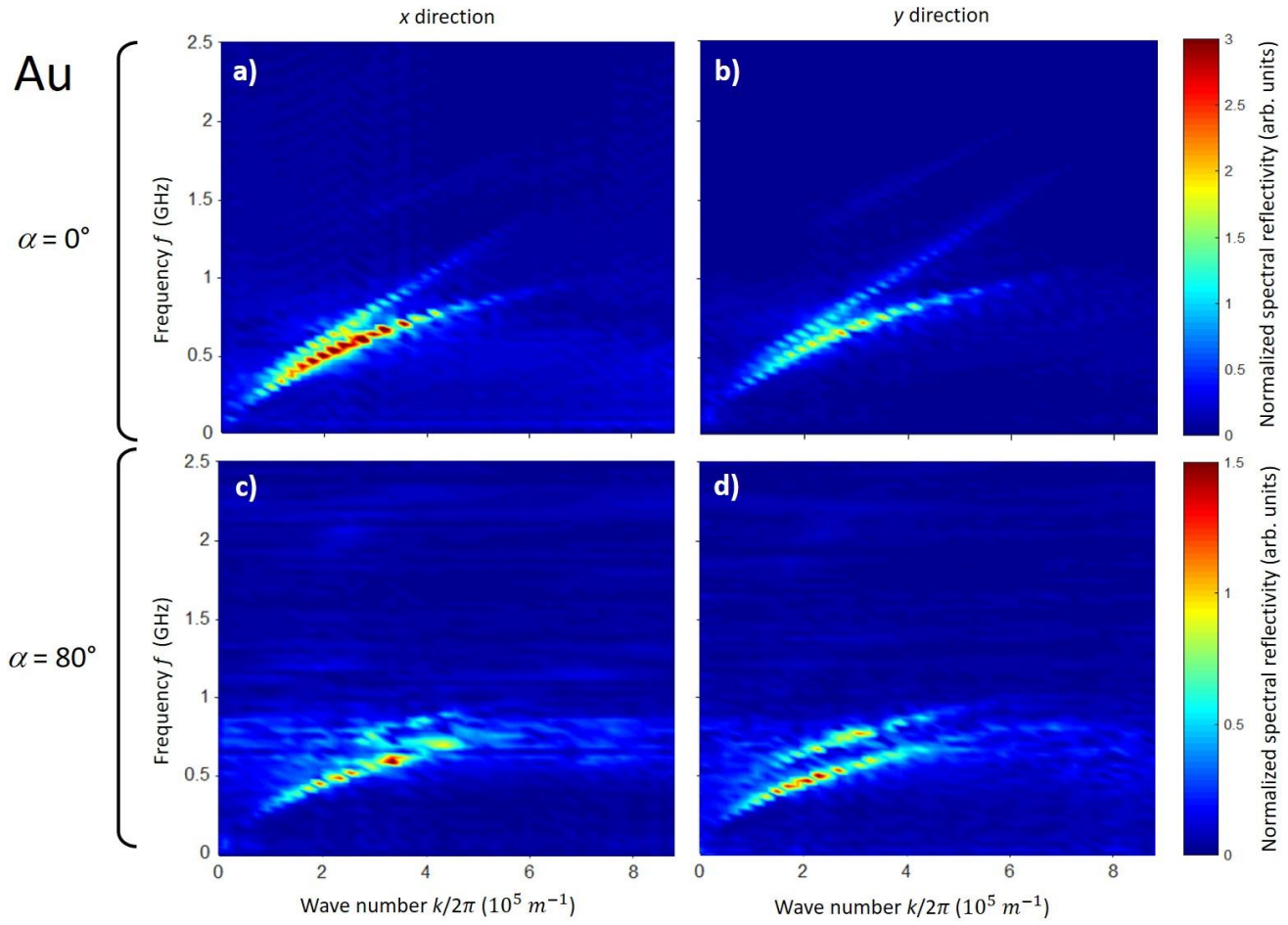

Fig. 6. Dispersion curves in Au films for x (a and c) and y (b and d) directions obtained from the variation of relative reflectivity vs. spatial and time frequencies for α = 0° (a and b) and α = 80° (c and d). The same procedure was used as in W films (Fig. 5) to determine the elastic wave group velocities, i.e. frequencies and wave numbers corresponding to the highest power spectral density (dark red level on normalized spectral reflectivity scale).

The group velocities v_x and v_y were calculated at the most intense normalized reflectivity of the pseudo-Rayleigh mode, which is at the wave number $k/2\pi = 3\times10^5$ m^{-1} in our case. Velocities are unsurprisingly very similar with $v_x = 1710$ m s^{-1} and $v_y = 1730$ m s^{-1} for Au films, and $v_x = 2220$ m s^{-1} and $v_y = 2260$ m s^{-1} for W films (Table 1).

These results support again the isotropic in-plane properties of films sputter-deposited at $\alpha = 0°$. It is important to remark that these velocities are always higher than the surface wave velocities of bulk metals (along the [100] crystallographic direction, $v_{Au} = 1124$ m s^{-1} and $v_W = 2646$ m s^{-1} from [53]) because of the silicon substrate for which $v_{Si} = 4917$ m s^{-1} along the [100] [53]. A Rayleigh wave propagates within a thickness of the order of the wavelength (the reciprocal of $k/2\pi$). The thinner the films, the bigger the substrate influences the wave velocity. Indeed, since the films thickness is 500 nm, the elastic properties of the substrate also contribute to the surface elastic wave propagation in the films (FEM simulations, not shown here with metallic films on silicon, give these velocity values). It is important to note that for W films, the measured velocity of the front of the wave (first detected crest) is in the order of 4000 m s^{-1} at a distance of 40 μm. Again, the silicon substrate influences the wave velocity by increasing the pseudo-Rayleigh wave velocity since the film thickness is only 500 nm.

Dispersion curves of GLAD films prepared with $\alpha = 80°$ are significantly different (Fig. 5c, d and 6c, d). The pseudo-Rayleigh waves remain the most intense propagative mode clearly measured with our pump-probe system. The slopes of the curves plotting frequency *vs.* wave number (therefore the group velocity) are lower than those measured with films produced by conventional sputtering process. The non-linear

evolution remains (dispersive materials) and the signal-to-noise ratio is lower. Indeed, increasing the incident angle favors the film roughness. It can start from a few nanometers and may be over tens of nanometers for films deposited with $\alpha > 85°$ [54, 55]. The beams power was lowered for GLAD W films in order to reduce W oxidation. However, the signal-to-noise ratio is significant enough to determine the velocity accurately for both metals. Following *x* and *y* directions, it simultaneously drops for Au films with v_x = 1230 m s^{-1} and v_y = 1180 m s^{-1}, whereas v_x = 920 m s^{-1} and v_y = 1640 m s^{-1} for W films, respectively (Table 1). For both metals, the drop is related to the voided microstructure produced with α = 80°. As commonly reported, the GLAD films density falls noticeably for grazing incident angles ($\alpha >$ 70°). From Grüner *et al.* [56], the film-to-bulk density ratio ρ_{film}/ρ_{bulk} as a function of the substrate tilt angle θ can be correctly estimated by:

$$\frac{\rho_{film}}{\rho_{bulk}} = \frac{H}{h}\cos\theta \qquad (2)$$

where *H* is the thickness of a film deposited at the same conditions under normal incidence (m), *h* the thickness of the porous film deposited onto the tilted substrate (m), and θ the substrate tilt angle (°) (α in our study). For an incident angle α = 80°, it gives ρ_{film}/ρ_{bulk} = 0.17 and 0.13 for Au and W films, which would mean that the voided fraction in the films is higher than 80%. Then, the elastic wave propagation is particularly disturbed at the columns interface due to this very porous microstructure.

It is also worth noting that the velocity falls more significantly following the *x* direction in W films with v_x = 920 m s^{-1} and v_y = 1640 m s^{-1}, whereas it is close to 1200 m s^{-1} in Au films for both directions (Table 1). This difference is again connected to the anisotropic porosity between *x* and *y* directions, which was previously evidenced from SEM pictures (Fig. 2a and b). Fanning of the column cross-section occurs in

W films (where the shadowing effect prevails) and gives rise to an elliptical shape with the long axis perpendicular to the plane of incidence of the particle flux. For GLAD Au films, shadowing effect still predominates but surface diffusion is less negligible compared to the deposition of W films. A porous microstructure is also produced with a more isotropic growth and thus, similar velocities in *x* and *y* directions.

In order to illustrate the directionally dependent properties in W and Au GLAD films, an anisotropic coefficient *A* defined as the *x*-to-*y* directions electrical resistivity (ρ_x/ρ_y) or velocity (v_x/v_y) ratio is plotted for both metals as a function of the incident angle α (Fig. 7).

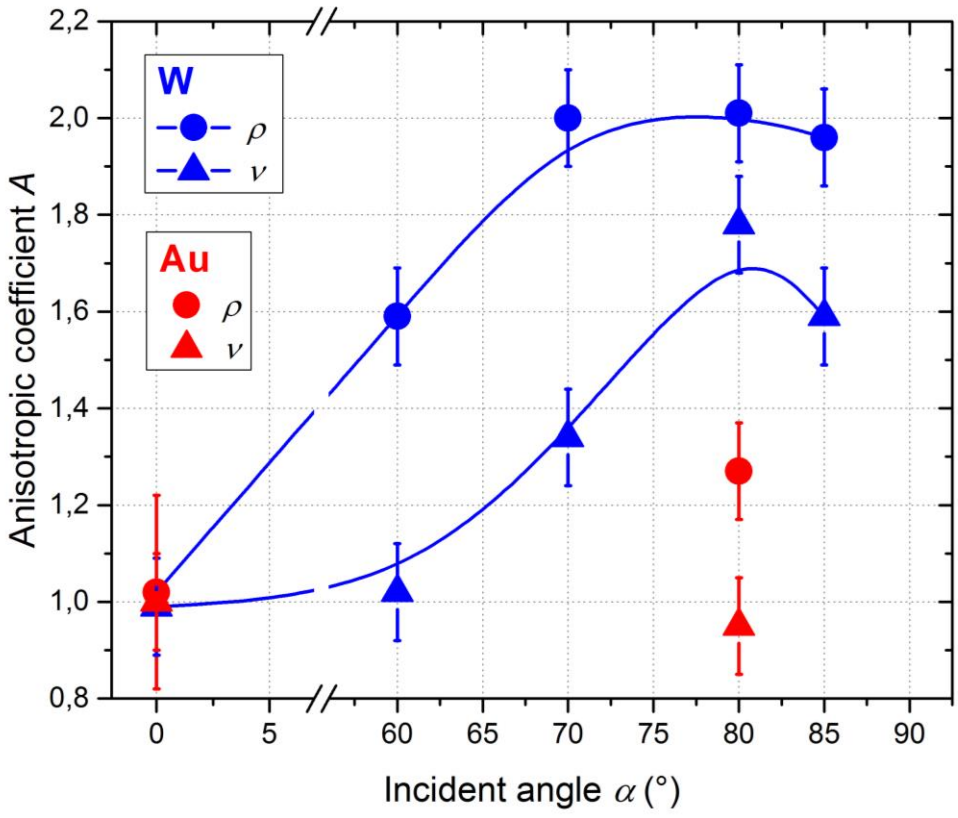

Fig. 7. Anisotropic coefficient as a function of the incident angle α in W and Au thin films. For DC electrical resistivity ρ and group velocity v of the pseudo-Rayleigh waves, each coefficient is defined as the ratio following the x and y directions.

For all Au films, resistivity and velocity anisotropic coefficients (A_ρ and A_v, respectively) are poorly influenced by α even for the most grazing angles. On the other hand, W GLAD films exhibit the most substantial variation of A_ρ and A_v *vs.* α, especially for incident angles higher than 60°. Resistivity anisotropic coefficients are systematically higher than velocity ones. This is closely connected to the influence of the substrate. Since films are deposited on glass substrate for resistivity and on (100) Si wafer for velocity measurements, the insulating substrate does not contribute to the electronic transport properties of GLAD films, whereas the silicon substrate increases the pseudo-Rayleigh wave velocity in both directions. Therefore, for higher incidence angles, the effect of the microstructural anisotropy is more evident on electrical resistivity than on elastic wave propagation. Increasing further the incident angle ($\alpha \geq 80°$) leads to nearly constant anisotropic coefficients since A_ρ tends to 2.0 and A_v is close to 1.8 in W films. The lateral growth producing a preferential bundling of the columnar microstructure in the *y*-direction saturates for the more oblique angles.

4 Conclusion

W and Au films were sputter-deposited by DC magnetron sputtering implementing the conventional process ($\alpha = 0°$) and the GLAD technique by changing the incident angle α up to 85°. Oriented columnar microstructures are produced with a tilt angle β achieving 41° and 57° for W and Au films prepared with an incident angle $\alpha = 80°$, respectively. For W films, an elliptical-shape of the cross-section is obtained

(fanning mechanism), whereas a more circular cross-section is produced for Au films due to surface diffusion. This diffusion process becomes significant for Au, whereas the shadowing effect prevails for W films.

Dense and crystallized W and Au films are grown by conventional sputtering, whereas they become porous and poorly crystallized when the incident angle is over 70°. Electrical resistivity abruptly rises for incident angles higher than 60° due to an increase of the voided microstructure. W films resistivity is more sensitive to the incident angle, which can be assigned to a more porous structure since shadowing effect predominates. On the other hand, surface diffusion cannot be neglected for Au films. These results correlate with the microstructural changes observed between W and Au GLAD films.

Elastic wave propagation is also influenced by the incident angle for both metallic films. A substantial drop of velocity (more than 25%) is systematically measured for W and Au GLAD films compared to those deposited by conventional sputtering. This drop is also due to the more voided microstructure produced in GLAD films, which prevents the elastic wave propagation at the column interfaces. Anisotropic resistivity and velocity are particularly evident in W GLAD films prepared for the highest incident angles. These asymmetric behaviors are due to the elliptical-shape of the W columns cross-section (fanning) created during the growth phase. For Au GLAD films, negligible anisotropic properties (resistivity and velocity) are measured, which is related to the more isotropic columnar microstructure. Our results demonstrate that the anisotropic microstructure plays a pivotal role in elastic wave propagation and electronic transport properties. The work presented in this paper also provides a typical example of how to tune directionally many physical characteristics of thin films and surfaces by means of a simple microstructural engineering approach.

Acknowledgements

This work was supported by the EIPHI Graduate School (contract ANR-17-EURE-0002), the Region of Franche-Comté and the French RENATECH network. This research was also sponsored by the French National Agency for Research (ANR) funds through the PHEMTO project.

References

[1] M. Lundstrom, Fundamentals of carrier transport, 2nd Ed., University Press, Cambridge, (2000). https://doi.org/10.1017/CBO9780511618611.

[2] D. Royer, E. Dieulesaint, Elastic waves in Solids I: Free and guided propagation, Springer-Verlag, Heidelberg, (2000). https://doi.org/10.1007/978-3-662-06938-7.

[3] F. Flory, L. Escoubas, G. Berginc, Optical properties of nanostructured materials: A review, J. Nanophotonics, 5 (2011) 052502-20. https://doi.org/10.1117/1.3609266.

[4] M.G. Stanford, P.D. Rack, D. Jariwala, Emerging nanofabrication and quantum confinement techniques for 2D materials beyond graphene, npj 2D Materials and Applications, 20 (2018) 1-15. https://doi.org/10.1038/s41699-018-0065-3.

[5] J. Rodriguez, M. Gomez, J. Ederth, G.A. Niklasson, C.G. Granqvist, Thickness dependence of the optical properties of sputter deposited Ti oxide films, Thin Solid Films, 365(1) (2000) 119-125. https://doi.org/10.1016/S0040-6090(99)01109-8.

[6] Y.Q. Fu, H.J. Du, S. Zhang, Functionally graded TiN/TiNi shape memory alloy films, Mater. Lett., 57(20) (2003) 2995-2999. https://doi.org/10.1016/S0167-577X(02)01419-2.

[7] S. Tawfick, M. De Volder, D. Copic, S.J. Park, C.R. Oliver, E.S. Polsen, M.J. Roberts, A.J. Hart, Engineering of micro- and nanostructured surfaces with anisotropic geometries and properties, Adv. Mater., 24 (2012) 1628-1674. https://doi.org/10.1002/adma.201103796.

[8] Z. Zeng, R. Liang, X.W. Li, S.P. Wen, Y. Gao, Y.L. Gu, F. Pan, Surface anisotropy of Cr_xN_{1-x} films prepared on an inner wall by magnetic sputtering, Appl. Surf. Sci., 253 (2007) 7563-7568. https://doi.org/10.1016/j.apsusc.2007.03.057.

[9] K. Robbie, M.J. Brett, A. Lakhtakia, Chiral sculptured thin films, Nature, 384(10) (1996) 616. https://doi.org/10.1038/384616a0.

[10] Y.P. Zhao, D.X. Ye, G.C. Wang, T.M. Lu, Designing nanostructures by glancing angle deposition, Proc. SPIE, 5219 (2003) 59-73. https://doi.org/10.1117/12.505253.

[11] C.M. Zhou, H.F. Li, D. Gall, Multi-component nanostructures design by atomic shadowing, Thin Solid Films, 517(3) (2008) 1214-1218. https://doi.org/10.1016/j.tsf.2008.05.049.

[12] I. Hodgkinson, Q.H. Wu, S. Collett, Dispersion equations for vacuum-deposited tilted-columnar biaxial media, Appl. Optics, 40 (2001) 452-457. https://doi.org/10.1364/ao.40.000452.

[13] D. Schmidt, Z.C. Kjerstad, T. Hofmann, R. Skomski, E. Schubert, M. Schubert, Optical, structural and magnetic properties of cobalt nanostructure thin films, J. Appl. Phys., 105 (2009) 113508-7. https://doi.org/10.1063/1.3138809.

[14] J. Dervaux, P.A. Cormier, P. Moskovkin, O. Douheret, S. Konstantinidis, R. Lazzaroni, S. Lucq, R. Snyders, Synthesis of nanostructured Ti thin films by combining glancing angle deposition and magnetron sputtering: A joint experimental and modeling study, Thin Solid Films, 636 (2017) 644-657. https://doi.org/10.1016/j.tsf.2017.06.006.

[15] P. Pedrosa, A. Ferreira, J.M. Cote, N. Martin, M. Arab Pour Yazdi, A. Billard, S. Lanceros-Mendez, F. Vaz, Influence of the sputtering pressure on the morphological features and electrical resistivity anisotropy of nanostructured titanium films, Applied Surface Science, 420 (2017) 681-690. https://doi.org/10.1016/j.apsusc.2017.05.175.

[16] R. El Beainou, N. Martin, V. Potin, P. Pedrosa, M. Arab Pour Yazdi, A. Billard, W-Cu sputtered thin films grown at oblique angles from two sources: Pressure and shielding effects, Surf. Coat. Technol., 343 (2018) 153-159. https://doi.org/10.1016/j.surfcoat.2017.09.062.

[17] P. Pedrosa, A. Ferreira, N. Martin, M. Arab Pour Yazdi, A. Billard, S. Lanceros-Mendez, F. Vaz, Nanosculptured Janus-like TiAg thin films obliquely deposited by GLAD co-sputtering for temperature sensing, Nanotechnol., 29 (2018) 355706-11. https://doi.org/10.1088/1361-6528/aacba8.

[18] H. Zhu, W. Cao, G.K. Larsen, R. Toole, Y. Zhao, Tilting angle of nanocolumnar films fabricated by oblique angle deposition, J. Vac. Sci. Technol., B30(3) (2012) 030606-4. https://doi.org/10.1116/1.4710999.

[19] E. Coffy, G. Dodane, S. Euphrasie, A. Mosset, P. Vairac, N. Martin, H. Baida, J.M. Rampnoux, S. Dilhaire, Anisotropic propagation imaging of elastic waves in oriented columnar thin films, J. Phys. D: Appl. Phys., 50 (2017) 484005-8. https://doi.org/10.1088/1361-6463/aa92ad.

[20] J.C. Sit, D. Vick, K. Robbie, M.J. Brett, Thin films microstructure control using glancing angle deposition by sputtering, J. Mater. Res., 14(4) (1999) 1197-1199. https://doi.org/10.1557/jmr.1999.0162.

[21] N. Martin, J. Sauget, T. Nyberg, Anisotropic electrical resistivity during annealing of oriented columnar titanium films, Mater. Lett., 105 (2013) 20-23. https://doi.org/10.1016/j.matlet.2013.04.058.

[22] J.A. Thornton, Influence of apparatus geometry and deposition conditions on the structure and topography of thick sputtered coatings, J. Vac. Sci. Technol., 11(4) (1974) 666-670. https://doi.org/10.1116/1.1312732.

[23] S. Mahieu, P. Ghekiere, D. Depla, R. De Gryse, Biaxial alignment in sputter deposited thin films, Thin Solid Films, 515(4) (2006) 1229-1249. https://doi.org/10.1016/j.tsf.2006.06.027.

[24] A. Anders, A structure zone diagram including plasma-based deposition and ion etching, Thin Solid Films, 518 (2010) 4087-4090. https://doi.org/10.1016/j.tsf.2009.10.145.

[25] R. Messier, A.P. Giri, R.A. Roy, Revised structure zone model for thin film physical structure, J. Vac. Sci. Technol., A2 (1984) 500-503. https://doi.org/10.1116/1.572604.

[26] S. Mukherjee, D. Gall, Structure zone model for extreme shadowing conditions, Thin Solid Films, 527 (2013) 158-163. https://doi.org/10.1016/j.tsf.2012.11.007.

[27] L. Abelmann, C. Lodder, Oblique evaporation and surface diffusion, Thin Solid Films, 305 (1997) 1-21. https://doi.org/10.1016/s0040-6090(97)00095-3.

[28] M. Drechsler, B. Blackford, A. Putnam, M. Jericho, A measurement of a surface self-diffusion coefficient by scanning tunneling microscopy, J. Phys. Colloques, 50 C8 (1989) 223-228. https://doi.org/10.1051/jphyscol:1989838.

[29] A. Piquet, H. Roux, V. T. Binh, R. Uzan, M. Drechsler, Une détermination du coefficient d'auto-diffusion de surface avec des pointes à émission de champ (tungstène), Surf. Sci., 44 (1974) 575-584. https://doi.org/10.1016/0039-6028(74)90138-1.

[30] A. Barranco, A. Borras, A.R. Gonzalez-Elipe, A. Palmero, Perspectives on oblique angle deposition of thin films: From fundamentals to devices, Prog. Mater. Sci., 76 (2016) 59-153. https://doi.org/10.1016/j.pmatsci.2015.06.003.

[31] D. Deniz, R.J. Lad, Temperature threshold for nanorod structuring of metal and oxide films grown by glancing angle deposition, J. Vac. Sci. Technol., A29 (2011) 011020-6. https://doi.org/10.1116/1.3525882.

[32] J.M. Garcia-Martin, R. Alvarez, P. Romero-Gomez, E. Cebollada, A. Palmero, Tilt angle control of nanocolumns grown by glancing angle sputtering of variable argon pressures, Appl. Phys. Lett., 97 (2010) 173103-3. https://doi.org/10.1063/1.3506502.

[33] R. Alvarez, J.M. Garcia-Martin, A. Garcia-Valenzuela, M. Macias-Montero, F.J. Ferrer, J. Santiso, V. Rico, J. Cotrino, A.R. Gonzalez-Elipe, A. Palmero, Nanostructured Ti thin films by magnetron sputtering at oblique angles, J. Phys. D: Appl. Phys., 49 (2016) 045303-10. https://doi.org/10.1088/0022-3727/49/4/045303.

[34] C. Charles, N. Martin, M. Devel, Optical properties of nanostructured WO_3 thin films by glancing angle deposition: Comparison between experiment and simulation, Surf. Coat. Technol., 276 (2015) 136-140. https://doi.org/10.1016/j.surfcoat.2015.06.051.

[35] D. Vick, T. Smy, M.J. Brett, Growth behavior of evaporated porous thin films, J. Mater. Res., 17(11) (2002) 2904-2911. https://doi.org/10.1557/jmr.2002.0421.

[36] T. Karabacak, G.C. Wang, T.M. Lu, Physical self-assembly and the nucleation of three-dimensional nanostructures by oblique angle deposition, J. Vac. Sci. Technol. A22(4) (2004) 1778-1784. https://doi.org/10.1116/1.1743178.

[37] T. Karabacak, J.P. Singh, Y.P. Zhao, G.C. Wang, T.M. Lu, Scaling during shadowing growth of isolated nanocolumns, Phys. Rev. B, 68 (2003) 125408-5. https://doi.org/10.1103/physrevb.68.125408.

[38] B.A. Belyaev, A.V. Izotov, P.N. Solovev, Growth simulation and structure analysis of obliquely deposited thin films, Russ. Phys. J., 59(2) (2016) 301-307. https://doi.org/10.1007/s11182-016-0771-2.

[39] M. Kardar, G. Parisi, Y.C. Zhang, Dynamic scaling of growing interfaces, Phys. Rev. Lett., 56 (1986) 889-892. https://doi.org/10.1103/physrevlett.56.889.

[40] A. van der Drift, Evolutionary selection, a principle governing growth orientation in vapour-deposited layers, Philips Res. Rep., 22 (1967) 267-268.

[41] F.A. Smidt, Use of ion beam assisted deposition to modify the microstructure and properties of thin films, Int. Mater. Rev., 35(2) (1990) 61-128. https://doi.org/10.1179/095066090790323975.

[42] F.T.N. Vüllers, R. Spolenak, Alpha- *vs.* beta-W nanocrystalline tungsten thin films: A comprehensive study of sputter parameters and resulting materials' properties, Thin Solid Films, 577 (2015) 26-34. https://doi.org/10.1016/j.tsf.2015.01.030.

[43] D. Choi, Phase transformation in thin tungsten films during sputter deposition, Microelectron. Eng., 183-184 (2017) 19-22. https://doi.org/10.1016/j.mee.2017.10.006.

[44] H.L. Sun, Z.X. Song, D.G. Guo, F. Ma, K.W. Xu, Microstructure and mechanical properties of nanocrystalline tungsten thin films, J. Mater. Sci. Technol., 26(1) (2016) 87-92. https://doi.org/10.1016/s1005-0302(10)60014-x.

[45] D.R. Lide (Ed.), CRC Handbook of Chemistry and Physics, Internet version, 2005, CRC press, Boca Raton, FL, 2005 (<http://www.hbcpnetbase.com>).

[46] D. Gall, Electron mean free path in elemental metals, J. Appl. Phys., 119(8) (2016) 052101-5. https://doi.org/10.1063/1.4942216.

[47] A. Besnard, N. Martin, L. Carpentier, B. Gallas, A theoretical model for the electrical properties of chromium thin films sputter deposited at oblique incidence, J. Phys. D: Appl. Phys., 44 (2011) 215301-8. https://doi.org/10.1088/0022-3727/44/21/215301.

[48] J. Lintymer, J. Gavoille, N. Martin, J. Takadoum, Glancing angle deposition to modify microstructure and properties of chromium thin films sputter deposited, Surf. Coat. Technol., 174-175 (2003) 316-323. https://doi.org/10.1016/s0257-8972(03)00413-4.

[49] D.M. Pandya, A.C. Rastogi, K.L. Chopra, Obliquely deposited amorphous Ge films. I Growth and structure, J. Appl. Phys., 46 (1975) 2966-2975. https://doi.org/10.1063/1.321984.

[50] A. Besnard, N. Martin, F. Sthal, L. Carpentier, J.Y. Rauch, Metallic to dielectric transition in titanium GLAD thin films sputter deposited, Funct. Mater. Lett., 6 (2013) 1250051-5. https://doi.org/10.1142/s1793604712500518.

[51] P. Pedrosa, J.M. Cote, N. Martin, M. Arab Pour Yazdi, A. Billard, In situ electrical resistivity measurements of vanadium thin films performed in vacuum during different annealing cycles, Rev. Sci. Instrum., 88 (2017) 025105-7. https://doi.org/10.1063/1.4974847.

[52] C. Song, G.K. Larsen, Y. Zhao, Anisotropic resistivity of tilted silver nanorod arrays: Experiments and modeling, Appl. Phys. Lett., 102 (2013) 233101-4. https://doi.org/10.1063/1.4809951.

[53] W.P. Mason, R.N. Thurston, Physical acoustics: Principles and methods, Academic Press, New York, 6 (1970) 136.

[54] J.L. Bubendroff, G. Garreau, S. Zabrocki, D. Berling, R. Jaafar, S. Hajjar, A. Mehdaoui, C. Pirri, Nanostructuring of Fe films by oblique incidence deposition on a $FeSi_2$ template onto Si(111): Growth, morphology, structure and faceting, Surf. Sci., 603(2) (2009) 373-379. https://doi.org/10.1016/j.susc.2008.11.026.

[55] M. Backholm, M. Foss, K. Nordlund, Roughness scaling in titanium thin films: A three-dimensional molecular dynamics study of rotational and static glancing angle deposition, Appl. Surf. Sci., 268 (2013) 270-273. https://doi.org/10.1016/j.apsusc.2012.12.077.

[56] C. Grüner, S. Liedtke, J. Bauer, S.G. Mayr, N. Rauschenbach, Morphology of thin films formed by oblique physical vapor deposition, ACS Nano Mater., 1 (2018) 1370-1376. https://doi.org/10.1021/acsanm.8b00124.